

From experimental data we would like to *visualize* the segment length distributions – in order both to gain some imagination of the *type*<sup>71</sup> of the distribution – and in order to understand the *arrangement of the domains* in the material. This visualization is achieved by computation of

- the chord length distribution (CLD) for general isotropic materials (Sect. 8.5.3)
- the interface distribution function (IDF) for 1D projections and the 1D scattering intensity of materials with a structure built from lamellae (Sect. 8.5.4)
- The multidimensional chord distribution function (CDF) for oriented materials (in particular useful for the study of materials with uniaxial orientation, i.e., fibers) (Sect. 8.5.5)

We notice that the 1D projections are perfect candidates for structure modeling by 1D models: arrange sticks in a row! For this purpose define stick-length distributions and the law of their arrangement. Fit such models to the measured scattering data (Sect. 8.7).

### 8.4.3.3 2D Projections

A well-known device that performs a 2D projection of the scattering pattern is the Kratky camera. By integrating the intensity along the direction of the focus slit, it is collapsing the SAXS intensity on the plane that is normal to the slit direction. In general, 2D projections collapse the measured complete intensity not on a line, but on a plane. As in the case of the 1D projections, the orientation of this plane can freely be chosen. The result of such a projection  $\{I\}_2(s_j, s_k)$  is not a curve as was the case with the 1D projection, but a 2D scattering pattern. Only in the case of 2D isotropy (i.e.,  $\{I\}_2(s_{jk})$  with  $s_{jk} = \sqrt{s_j^2 + s_k^2}$ ) the scattering pattern can be *represented* by a curve.

Such 2D isotropy is fulfilled in the case which is of the highest practical value. Here the 2D projection

$$\{I\}_2(s_{12}) = 2 \int_0^\infty I(s_{12}, s_3) ds_3 \quad (8.58)$$

describes BONART's [16] transversal structure of a fiber – the arrangement of domain cross-sections in the fiber cross-section. Figure 8.18 demonstrates the structure. In analogy to the 1D projections, chords can be imagined to penetrate the representative cross-section “in the plane”. They become segmented by the circular domain cross-sections. Finally the segment length distributions generate  $\{I\}_2(s_{12})$ .

## 8.5 Visualization of Domain Topology from SAXS Data

After we have discussed the composition parameters of the SAXS of a multiphase material, we now start with the investigation of the topology. The most simple access to the arrangement of domains in the material is the discussion of long period

<sup>71</sup> Are the distributions Gaussians, Lorentzians, or even more complex?

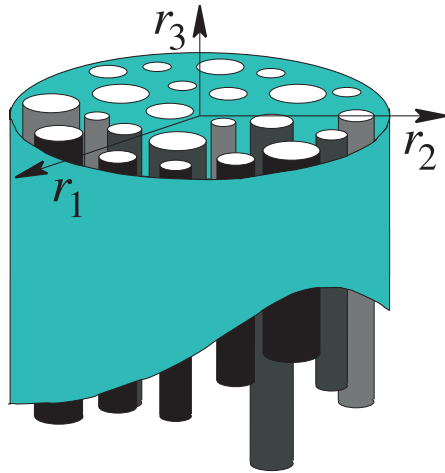


**Figure 8.18.** Transversal structure of a fiber. The topological information on the structure of a fiber that is related to the 2D projection  $\{I\}_2(s_{12})$  contains structure information from the representative cross-sectional plane  $(r_1, r_2)$  of the fiber. Size distribution and arrangement of the domain cross-sections are revealed

peaks (cf. Sect. 8.2.6). The next level of analysis is visualization of topology. Only for nearly monodisperse or highly oriented materials we should skip this step and directly proceed to a modeling of the structure and fitting of the scattering data<sup>72</sup>. As we have just learned, topology information is only a part of the information buried in a SAXS pattern. So before topology can be visualized, the respective information must be extracted from the scattering pattern.

### 8.5.1 Extraction of the Topological Information

For the scattering of an isotropic material we already know the result of the separation and a method to obtain it: the result is the scattering of the ideal multiphase system as sketched on p. 123 in Fig. 8.9. A way to obtain the result is the classical Porod-law analysis (Sect. 8.3.2).

The fundamental problem of the classical method is the fact that there is no viable<sup>73</sup> procedure to extend it to the scattering of anisotropic materials. Moreover, the required manual processing is cumbersome, slow and may yield biased results.

**The Interference Function.** The function sketched in Fig. 8.9 can be understood as  $s^p I_{id}(s)$ , the intensity of the *ideal* multiphase system multiplied by a power

<sup>72</sup>The background for this advice is explained in the discussion of Fig. 8.35, p. 162.

<sup>73</sup>Conceded – we can successively project anisotropic data to different directions, carry out the manual procedure for each direction, and, finally recombine the curves. But even if we replace the manual procedure by an automated one, the combination of curves turns out to be not contiguous: There is no smooth surface anymore.

$p$  of the modulus of the scattering vector. In the example  $p = 4$  compensates the decay of the Porod law. The scattering intensity of the ideal multiphase system is readily obtained by dividing the result of the Porod-law analysis by  $s^p$ .  $I_{id}(s)$  is the starting point for nanostructure visualization by means of the correlation function (cf. Sect. 8.5.2). By a small modification we obtain a well-behaved function

$$G_1(s) = s^p I_{id}(s) - A_p, \quad (8.59)$$

as it is vanishing in the limit

$$\lim_{s \rightarrow \infty} G_1(s) = 0.$$

Equation (8.59) defines the 1D *interference function* of a layer stack material.  $G_1(s)$  is one-dimensional, because  $p$  has been chosen in such a way that it extinguishes the decay of the Porod law. Its application is restricted to a layer system, because misorientation has been extinguished by LORENTZ correction. If the intensity were isotropic but the scattering entities were no layer stacks, one would first project the isotropic intensity on a line and then proceed with a Porod analysis based on  $p = 2$ . For the computation of multidimensional anisotropic interference functions one would choose  $p = 2$  in any case, and misorientation would be kept in the state as it is found. If one did not intend to keep the state of misorientation, one would first desmear the anisotropic scattering data from the orientation distribution of the scattering entities (Sect. 9.7).

The addressed types of interference functions are the starting point for the evaluations described in Sects. 8.5.3-8.5.5.

**Automated Extraction of Interference Functions.** For the classical synthetic polymer materials it is, in general, possible to strip the interference function from the scattering data by an algorithm that does not require user intervention. Quantitative information on the non-topological parameters is lost (STRIBECK [26, 153]). The method is particularly useful if extensive data sets from time-resolved experiments of nanostructure evolution must be processed. Background ideas and references are presented in the sequel.

Concerning the notions on the deviations of the real structure from an ideal multiphase topology, a survey shows that all models are resulting in *slowly varying* backgrounds of the scattering pattern. On the other hand, noise originating from counting statistics is displaying *high-frequency* deviations of the measured signal from the smooth shape of the scattering. If we are investigating polydisperse soft materials, the observed reflections are broad, i.e., they do not contain high spatial frequencies. Under these conditions the extraction of the topological information can be considered a problem of *signal processing*. The power spectrum of the measured SAXS data shows three distinct bands: backgrounds are in the low spatial frequencies, in the high spatial frequencies there is only noise (because of lacking long-range order) – and the spatial frequency band of polydisperse topology is in between. Thus background can be removed from the scattering pattern by spatial frequency filtering

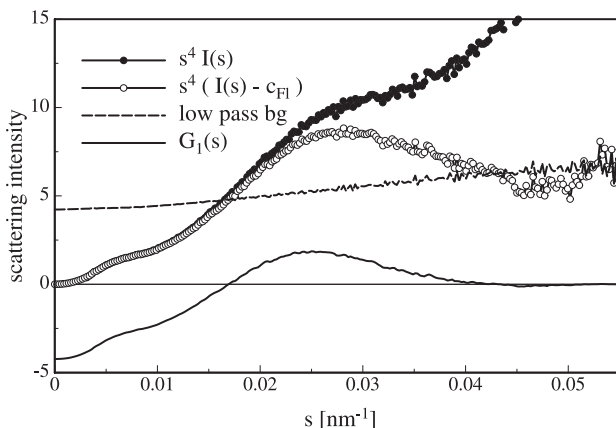


**Figure 8.19.** Extraction of the scattering of an ideal two-phase structure from the raw scattering data of an isotropic UHMWPE material by means of spatial frequency filtering

returning an interference function  $G_f(s) \approx mG(s)$  with  $m < 1$  being an unknown factor that describes some loss in the filter, and  $G(s)$  the true interference function.

We observe that this method works for data of any dimensionality. Figure 8.19 demonstrates the extraction of the interference function for the case of an isotropic ultra-high molecular-weight polyethylene material. From the raw data (filled circles) a constant fluctuation background estimate<sup>74</sup>  $c_{FI}$  is subtracted in order to ease the task of the filter. The background obtained by low-pass filtering is the dashed line. After subtraction of the background and multiplication by the “Cosine-bell function” (Hanning filter) [26, 153, 154] the interference function (solid line) is received<sup>75</sup>.

It is clear that this procedure can be iterated. Iteration successively improves the “balance” of the interference function – and theory says that  $\int G(s) ds = 0$  should be perfectly balanced if the domain surfaces (e.g., the surfaces of the crystalline lamellae) are smooth. Thus we can interpret iterative spatial frequency filtering as a method to remove the effect of a rough phase boundary. Inevitably this goes along with the extinction of the scattering effect of small domains (e.g., small crystallites). Therefore, removing roughness by iterative spatial frequency filtering is only a last resort for those few materials with very rough [155] domain boundary.

<sup>74</sup>See p. 118, Fig. 8.8 and the corresponding comparison of soft matter and metals: Subtract 90% of the intensity minimum.

<sup>75</sup>Assistance of how to choose and to write the low pass filter, the use of the Hanning filter, etc., can be found in textbooks of digital image processing or in the “Reference Guide” of *pv-wave*. A command (#FILTINT) to carry out spatial frequency filtering of scattering curves is part of my program TOPAS. If fiber patterns shall be evaluated, a *pv-wave* procedure `sf_interfer` does the main job. Both examples are available as source codes (cf. p. 29).

### 8.5.2 1D Correlation Function Analysis

The easiest way to get some impression of the structure behind our scattering data without resorting to models is the computation and interpretation of a correlation function. We will mainly discuss the 1D correlation function,  $\gamma_1(r_3)$ , because any slice of an anisotropic correlation function is a one-dimensional correlation function. Moreover,  $\gamma_1(r_3)$ , is readily describing the topology of certain frequent structural entities (stacks made from layers and microfibrils). There is an advantage of the correlation function analysis as compared to “long period interpretation”. The analysis of the correlation function permits to determine the *average domain thicknesses* (for example the thicknesses of crystalline and amorphous layers). The principal disadvantage of the correlation function is the fact that polydispersity is not properly reflected in the correlation function [2]. This means that the statistics of domain thickness variation is very difficult to study from a correlation function. In particular, for the latter purpose it is more appropriate to carry out an analysis of the IDF or of the CDF.

**1D Structural Entities.** In materials science, structural entities which can satisfactorily be represented by layer stacks are ubiquitous. In the field of polymers they have been known for a long time [156]. Similar is the microfibrillar [157] structure. Compared to the microfibrils, the layer stacks are distinguished by the large lateral extension of their constituting domains. Both entities share the property that their two-phase structure is predominantly described by a 1D density function,  $\Delta\rho(r_3)$ , which is varying along the principal axis,  $r_3$ , of the structural entity.

**1D Intensity.** As already mentioned (cf. p. 126 and Fig. 8.12), the isotropic scattering of a layer-stack structure is easily “desmeared” from the random orientation of its entities by LORENTZ correction (Eq. 8.44). For materials with microfibrillar structure this is more difficult. Fortunately microfibrils are, in general, found in highly oriented fiber materials where they are oriented in fiber direction. In this case the one-dimensional intensity in fiber direction,

$$I_1(s_3) = 2\pi \int_0^\infty s_{12} I(s_{12}, s_3) ds_{12},$$

can directly be interpreted as the 1D intensity of the microfibrils along their principal axis. By projecting we loose the information on the thickness of the microfibrillar strands and on possible lateral correlations among them.

**Warning.** For isotropic materials the 1D projection  $\{I\}_1$  and the LORENTZ correction yield different 1D intensities. Both are related by

$$I_1(s) = 2\pi s^2 I(s) = -s \frac{d}{ds} [\{I\}_1(s)]. \quad (8.60)$$

Model functions for the 1D intensity have early been developed [128, 158] and fitted to scattering data. The classical model-free structure visualization goes back to

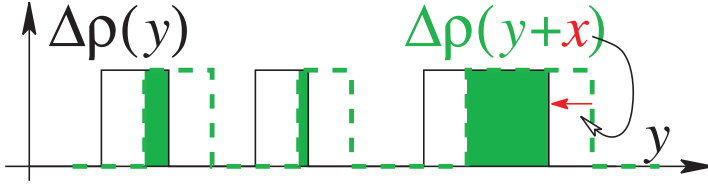


**Figure 8.20.** Generation of a 1D correlation function,  $\gamma_1(x)$ , by autocorrelation of the 1D electron density,  $\Delta\rho(y)$  for a two-phase topology. Each value of  $\gamma_1(x)$  is proportional to the overlap integral (total shaded area) of the density and its displaced ghost

VONK [159, 160] and describes the structure by the 1D correlation function  $\gamma_1(r_3)$  in physical space.

**Computation of a 1D Correlation Function.** Each *one*-dimensional correlation function,  $[\gamma]_1(x)$  or  $\gamma_1(x)$  (with  $x = r_3$ )

$$[\gamma]_1(x) = \frac{2}{k} \int_0^\infty \{I\}_1(s) \cos(2\pi xs) ds \quad (8.61)$$

$$\gamma_1(x) = \frac{2}{k} \int_0^\infty I_1(s) \cos(2\pi xs) ds \quad (8.62)$$

$$= \frac{4\pi}{k} \int_0^\infty s^2 I(s) \cos(2\pi xs) ds \quad (8.63)$$

is computed from its 1D intensity,  $\{I\}_1(s)$  or  $I_1(s)$ , by a *one*-dimensional Fourier transform. Equation (8.63) is valid<sup>76</sup> for the isotropic scattering of a lamellar multi-phase system.

Numerically the correlation function is easily computed, after either a classical POROD-law analysis has been carried out (Sect. 8.3.2), or the interference function has been obtained by spatial frequency filtering (p. 140). For the purpose of extending the integral we may write an adapted Fourier-transformation algorithm which explicitly utilizes the analytical continuation according to POROD's law, or we may use the continuation for the generation of additional grid points and employ the discrete fast Fourier transformation (DFFT) algorithm [154, 161].

Figure 8.20 demonstrates the generation of  $\gamma_1(x)$  by displacement of the 1D electron density<sup>77</sup>,  $\Delta\rho(y)$ , with respect to its ghost,  $\Delta\rho(y+x)$ , along the stack axis  $y$ . The direction  $x$  in the sketch is identical to the direction of the stack normal,  $r_3$ , in Fig. 8.12 on p. 126. The sketch depicts a displacement  $x$  that is still so small that each domain is only correlated to itself (shaded areas). At such a position  $x$  we are still in

<sup>76</sup>The presented result is different from the *radial correlation function*  $\gamma(r) = 4\pi \int s^2 I(s) (\sin(2\pi rs)/2\pi rs) ds$ , which is computed from the isotropic scattering intensity by means of the *three*-dimensional Fourier transform.

<sup>77</sup>For the sake of simplified presentation here, it is assumed that there are only few scattering entities in a sea of matrix material, and the average  $\langle\rho\rangle_V \approx \rho_1$  is close to the density of the matrix phase

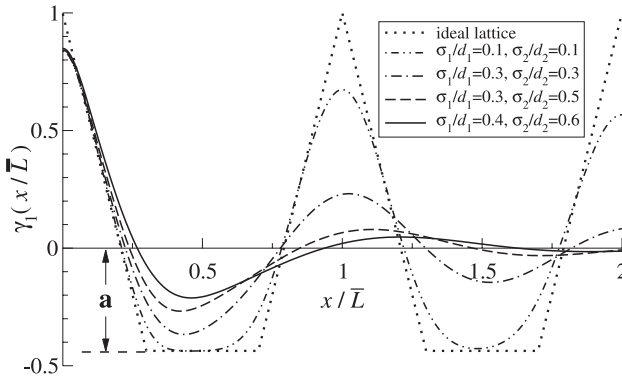


**Figure 8.21.** Features of a 1D correlation function,  $\gamma_1(x/\bar{L})$  for perfect and disordered topologies.  $\bar{L}$  is the number-average distance of the domains from each other (i.e., long period). *Dotted*: Perfect lattice. *Dashed and solid lines*: Paracrystalline stacks with increasing disorder.  $a = -v_{l_1}/(1 - v_{l_1})$  with  $0 < v_{l_1} \leq 0.5$  is a measure of the linear volume “crystallinity” in the material, which is either  $v_{l_1}$  or  $1 - v_{l_1}$

the region of linear decay of the correlation function, i.e., in the so-called “autocorrelation triangle”. The typical shape of such a correlation function for topologies with varying amount of disorder is sketched in Fig. 8.21. Obviously, the autocorrelation triangle of the ideal lattice (dotted curve) is not preserved in paracrystalline stacks of higher polydispersity. Thus, a simple linear extrapolation (“linear regression autocorrelation triangle”, LRAT [162]) will only yield reliable information concerning the properties of the idealized lattice from the real data, if the polydispersity remains rather low.

**Analysis of the 1D Correlation Function.** Several publications describe the search for a simple *graphical* analysis [22, 159, 162–164] of the 1D correlation function by means of a geometrical construction. It is the drawback of all such methods that polydispersity and heterogeneity are not considered. The methods are derived from the general generation principle of correlation functions (Fig. 8.20), resulting in equations (cf. Eqs. (8.23), (8.70) and (8.64)) for the first off-origin maximum, the depth of the first minimum or the *initial slope*  $\gamma'_{id}(0)$  of ideal correlation functions. For the simplified case of a lamellar system we obtain

$$\gamma_{1,id}(x) = 1 - \frac{1}{\ell_{p1}} |x| + \dots \quad (8.64)$$

with  $\ell_{p1}$  being the average chord length of the one-dimensional ideal two-phase topology with

$$\frac{1}{\ell_{p1}} = \frac{1}{\bar{d}_1} + \frac{1}{\bar{d}_2}, \quad (8.65)$$

$\bar{d}_1$  the average layer thickness of the first of the two kinds<sup>78</sup> of lamellae, and  $\bar{d}_2$  related to the second kind of layers.  $\bar{L} = \bar{d}_1 + \bar{d}_2$  is called the average<sup>79</sup> long period. Without loss of generality we may restrict further discussion to *linear crystallinities*<sup>80</sup>

$$v_l = \frac{\bar{d}_1}{\bar{L}} \quad (8.66)$$

with  $v_l \leq 0.5$ . The crystallinity is called “linear” in order to distinguish it from the overall volume crystallinity in the sample, because  $v_l$  does not account for the presence of extended domains (of matrix material) outside the scattering entities. From Eqs. (8.64) and (8.65) we obtain for the zero of the initial slope of the ideal correlation function

$$\begin{aligned} x_0 &= \frac{\bar{d}_1 \bar{d}_2}{\bar{d}_1 + \bar{d}_2} \\ &= v_l (1 - v_l) \bar{L}. \end{aligned} \quad (8.67)$$

Figure 8.21 shows model functions both for ideal and realistic cases. The dotted curve demonstrates the case of the ideal and infinitely extended 1D lattice. Here every time the ghost is displaced by an integer multiple of the lattice constant ( $x/L = 1, 2, 3, \dots$ ), the correlation returns to the ideal value 1. For the 1D lattice not only  $x_0$ , but also the valley depths

$$\gamma_{l,min} = a = -\frac{v_l}{1 - v_l} \quad (8.68)$$

are related to the composition<sup>81</sup>,  $v_l(1 - v_l)$ , of the material (see also p. 133, Fig. 8.15). The common graphical evaluation methods try to transfer these features of the ideal correlation function of an ideal lattice to real correlation functions of polydisperse soft matter that are computed from experimental data. The valley-depth method has first been devised by VONK [159]: whenever a flat minimum is found in a real correlation function, the distortion is weak and the linear crystallinity can significantly be determined from the properly normalized correlation function by application of Eq. (8.68).

In practice, the observed distortion is frequently strong. Thus, the correlation-function minimum is not flat. This is demonstrated in most of the dashed and solid curves in Fig. 8.21. They show model correlation functions of the paracrystalline stacking model with varying amount of disorder. Computation<sup>82</sup> is based on Eq. (8.104), p. 180.

<sup>78</sup>For instance the “amorphous”, “hard”, “crystalline”, ...

<sup>79</sup>Speaking of averages and denoting symbols by an overbar already means a generalization for distorted structures which will be discussed later.

<sup>80</sup>Again, “crystallinity” may be replaced by “hard phase fraction”, “soft phase fraction”, or whatever designation applies better to the material that is studied.

<sup>81</sup>Conceded – Eq. (8.68) violates Babinet’s theorem. Nevertheless, it is valid for  $v_l \leq 0.5$  and can easily be remembered, whereas the correct equation is somewhat more involved.

<sup>82</sup>It is convenient to set  $A_{P_1} = 1$ ,  $\bar{L} = \bar{d}_1 + \bar{d}_2 = 1$ . Rounding errors are suppressed by replacing the intensity by  $1/s^2$  (POROD’s law) for big arguments ( $s > 8$ ). A smooth phase transition zone (in all the example curves:  $d_z = 0.1$ ) is considered by multiplication with  $\exp\left(-(2\pi s d_z/3)^2\right)$ . From this one-dimensional scattering intensity the correlation function is obtained by Fourier transformation.



Figure 8.21 shows functions of the distorted topologies that are *not pointed at the origin*, and  $\gamma_1(0) < 1$ . The reason is that the presented model is not an ideal two-phase system, because it considers smooth transitions of the electron density between the “crystalline” and the “amorphous” layers.

In practice, even a *more severe damping* of the correlation function close to the origin is *frequently accepted* in order to compute the correlation function with little effort of evaluation [159]: POROD’s law is not evaluated (cf. p. 124, Fig. 8.11), and thus the Fourier integral cannot be extended to infinity. Instead, the position  $s_{min}$  in the scattering curve is determined at which the SAXS intensity is lowest. This level is subtracted, and the integral is only extended up to  $s_{min}$ .

The case of low distortion is shown in the dashed-dotted-dotted curve from Fig. 8.21. The first minimum still reaches the ideal valley depth. Therefore it is still possible to determine the linear composition of the material from Eq. (8.68).

Let us discuss the first off-origin maximum of  $\gamma_1(x/\bar{L})$ . For the ideal lattice and weakly distorted materials the maximum is found at the position of the number-average long period,  $\bar{L}$ , i.e. at  $x/\bar{L} = 1$ . This is not the case for structures that are distorted more severely. Thus a long period,  $\bar{L}_{app}$ , determined from the position of the first maximum in  $\gamma_1(x)$  is only an apparent one, and it is always overestimated [130]. An overestimation of 20% ( $\bar{L}_{app} \approx 1.2\bar{L}$ ) is not unusual.

**The First-Zero Method of Correlation Function Analysis.** For the purpose of a practical graphical evaluation of the linear crystallinity, Eq. (8.67) can be applied to a *renormalized* correlation function  $\gamma_1(x/\bar{L}_{app})$ . The method which has been proposed by Goderis et al. [162] is based on the implicit assumption that the first zero,  $x_0$ , of the real correlation function is shifted by the same factor as is the position of its first maximum,  $\bar{L}_{app}$ .

The idea is already described in the first paper of VONK and KORTLEVE ([159], p. 22) as a method to retrieve fit parameters. In their second paper ([160], p. 128) the authors state that inaccurate values are returned, if the found linear crystallinity is between 0.35 and 0.65.

The general inferiority of geometrical construction methods [162, 163] as compared to more involved methods which consider polydispersity has first been demonstrated by SANTA CRUZ et al. [130], and later in many model calculations by CRIST [165–167]. Nevertheless, in particular the first-zero method is frequently used. Thus, it appears important to assess its advantages as well as its limits. Validation can be carried out by graphical evaluation of model correlation functions [130, 165].

If the statistical model of a *paracrystalline stack* is assumed, it turns out that the renormalization attenuates the influence of polydispersity on the position of the first zero. In general, the first-zero method is more reliable than the valley-depth method, although it is not perfect. Even the first-zero method is overestimating the value of  $v_l$ . The deviation is smaller than 0.05, if the found crystallinity is smaller than 0.35. If bigger crystallinities are found, the significance of the determination is

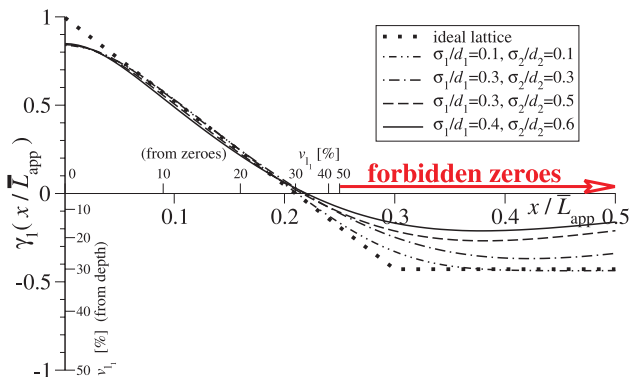


**Figure 8.22.** Testing the first-zero method for the determination of the linear crystallinity,  $v_l$ , from the linear correlation function,  $\gamma_l(x/\bar{L}_{app})$  with  $\bar{L}_{app}$  being the position of the first maximum in  $\gamma_l(x)$  (not shown here - but cf. Fig. 8.21). Model tested: Paracrystalline stacking statistics with Gaussian thickness distributions. The interval of forbidden zeroes is shown. An additional horizontal non-linear axis permits to determine the linear crystallinity directly. A corresponding vertical axis shows the variation of the classical “valley-depth method”

rapidly breaking down, and an individual demonstration of the error of determination becomes essential. In practice, insignificance can no longer be overlooked, if Eq. (8.69) applied to measured data does not return real solutions (“forbidden zeroes” in Fig. 8.22).

If the initial part of the correlation function exhibits significant deviations from a straight line, the proposers of the first-zero method recommend to carry out a linear regression (LRAT) [162] on the autocorrelation triangle. The problem of doing so is demonstrated in Fig. 8.21 and its discussion. Moreover, if the initial part of the correlation function does not only show a monotonous decay but discrete features, this is a strong indication of a topology that is not only polydisperse, but also heterogeneous<sup>83</sup>. In this case, a graphical correlation function analysis of isotropic data is of little significance anyway, and the study of uniaxially oriented material is recommended. Analysis may be performed by means of the CDF method (cf. Sect 8.5.5). If a low-noise scattering curve from isotropic material is at hand, it may be possible to separate components of a heterogeneous nanostructure by means of the IDF method (cf. Sect. 8.5.4) combined with model fits.

The first-zero method starts from the ideal lattice and Eq. (8.67). For the purpose of evaluation of scattering curves from polydisperse soft matter the ideal long period,  $\bar{L}$ , is replaced by  $\bar{L}_{app}$ , i.e. the validity of  $\gamma_l(v_l(1-v_l)\bar{L}_{app}) = 0$  is assumed. Because of the fact that the zero of a function is determined, not even a normalization of  $\gamma_l(x)$  is required [162]. Figure 8.22 displays the model data of Fig. 8.21 after the method-inherent renormalization  $x \rightarrow x/\bar{L}_{app}$ . Comparison with Fig. 8.21 shows that now

<sup>83</sup>No infinitely extended layers, several components with different topology (e.g. primary and secondary lamellar stacks)

the zeroes of the correlation functions with varying polydispersity are found close to the correct value  $x_0/\bar{L}_{app} = 0.21 = 0.3(1 - 0.3)$ . Vice versa, a good estimate for the linear crystallinity is obtained from the pair of roots which solve the quadratic relation

$$\frac{x_0}{\bar{L}_{app}} = v_{lc}(1 - v_{lc}). \quad (8.69)$$

If other statistical models of polydispersity should prove more appropriate than the paracrystalline stack, validations of the first-zero method may be carried out in analogy to the one presented here.

For anisotropic scattering patterns and the multidimensional case VONK ([168] and [22], p. 302) has proposed to utilize a *multidimensional* correlation function. It is not frequently applied.

### 8.5.3 Isotropic Chord Length Distributions (CLD)

The isotropic chord length distribution (CLD) is of limited practical value if soft matter with only short-range order is studied. Nevertheless, the related notions have been fruitful for the development of new methods for topology visualization from SAXS data.

**Related Notions.** Not only the 1D correlation function, but also the general 3D correlation function starts with a linear decay, and its series expansion

$$\gamma(r) = 1 - \frac{|r|}{\ell_p} + \dots \quad (8.70)$$

was already given by POROD [18].  $\ell_p$  is the average chord length that has already been introduced on p. 112 in Eq. (8.23). Starting from this relation MÉRING and TCHOUBAR [118, 141, 169, 170] have derived that even the *distributions* of the individual segment lengths can be visualized by evaluation of an isotropic scattering pattern. They make use of the derivation theorem (p. 23, Eq. 2.39) applied to deliberate slicing directions of the structure and apply it twice. The two derivatives are distributed on each of the factors of the autocorrelation,  $\Delta\rho^{*2}(r)$ , and an ideal *edge enhancement* is accomplished. The result shows that the second radial derivative of the radial correlation function

$$\gamma''(r) = \frac{1}{\ell_p} (-2\delta(r) + g(r) + g(-r)) \quad (8.71)$$

is formed by two images of a *chord length distribution* (CLD),  $g(r)$  and a  $\delta$ -distribution at the origin (Fig. 8.23). The CLD is made from an infinite series of segment distributions that starts with the homo-segment distributions,  $\ell_1(r)$  and  $\ell_2(r)$ , for the domains of phase 1 and 2, respectively<sup>84</sup>, followed by the di-segment distributions of the long periods,  $-2\ell_{12}(r)$ , and further out by the multi-segment distributions which describe the long-range arrangement of the particles in the material.

<sup>84</sup>Shape and size of the domains make these distributions.

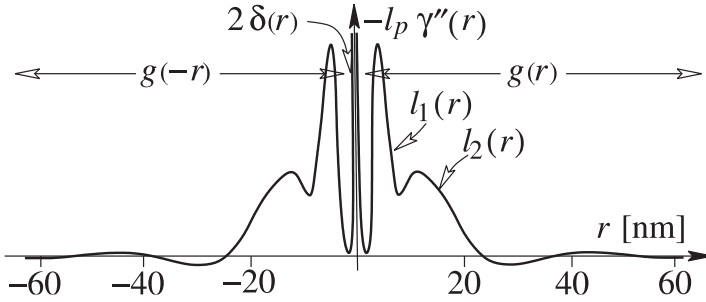


**Figure 8.23.** The chord length distributions  $g(r)$  and  $g(-r)$  found in the 2nd derivative  $\gamma''(r)$  of the radial correlation function. The example shows  $g(r)$  of a suspension of 10 wt.-% of silica (reproduced from a handout of DENISE TCHOUBAR)

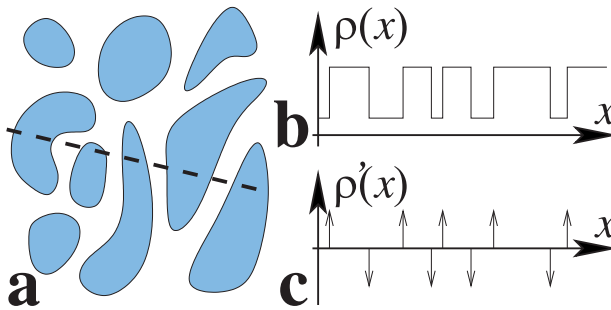


**Figure 8.24.** Demonstration of the edge-enhancement principle built into the chord length distribution. (a) Two-phase structure intersected by a straight line. (b) The density along the line. (c) The derivative of the density is a sequence of  $\delta$ -functions which are marking the positions of the domain edges

In the sketch taken from a handout of TCHOUBAR the distributions  $\ell_1(r)$  and  $\ell_2(r)$  are separated extraordinarily well.

The relation between structure and the chord distributions is readily established from considerations of topological density functions along a straight line traversing the material (Fig. 8.24). In Fig. 8.24a the respective sequence of chords is indicated. Figure 8.24b is a sketch of the corresponding density function,  $\rho(x)$ . Its first derivative,  $\rho'(x)$  (Fig. 8.24c), is nothing but a sequence of  $\delta$ -functions put at the positions of the domain edges. Thus the edges are enhanced, and the autocorrelation  $-\rho'(x) \star \rho'(-x) = g_p(x)$  is the partial CLD for the chosen special path through the topology.

For a general, isotropic and condensed multiphase material with short-range order, the CLD offers the best possible model-free visualization of the nanostructure. Nevertheless, the image does not show many details because of the inherent solid-angle average.

### 8.5.4 1D Interface Distribution Functions (IDF)

**Opportunities and Limits.** If we intend to obtain a clearer look on nanostructure than the one the CLD is able to offer, we can try to get rid of the orientation smearing – either by considering materials with a special topology (layer stacks), or by studying anisotropic materials.

If the scattering entities in our material are *stacks of layers with infinite lateral extension*, Eq. (8.47) is applicable. This means that we can continue to investigate isotropic materials, and nevertheless unwrap the 1D intensity of the layer stack. To this function RULAND applies the edge-enhancement principle of MÉRING and TCHOUBAR (cf. Sect. 8.5.3) and receives the interface distribution function (IDF),  $g_1(x)$ . Ruland discusses isotropic [66] and anisotropic [67] lamellar topologies.

For a layer-stack material like polyethylene or other semicrystalline polymers the IDF presents clear hints on the shape of the layer thickness distributions, the range of order, and the complexity of the stacking topology. Based on these findings inappropriate models for the arrangement of the layers can be excluded. Finally the remaining suitable models can be formulated and tested by trying to fit the experimental data.

As pointed out by STRIBECK [139, 171]  $g_1(x)$  is, as well, suitable for the study of oriented microfibrillar structures and, generally, for the study of 1D slices in deliberately chosen directions of the correlation function. This follows from the Fourier-slice theorem and its impact on structure determination in anisotropic materials, as discussed in a fundamental paper by BONART [16].

In practical application to common isotropic polymer materials the IDF frequently exhibits very broad distributions of domain thicknesses. At the same time fits of the IDF curve to the well-known models for the arrangement of domains (cf. Sect. 8.7) are not satisfactory, indicating that the existing nanostructure is more complex. In this case one may either fit a more complex model<sup>85</sup> on the expense of significance, or one may switch to the study of anisotropic materials and display their nanostructure in a multidimensional representation, the multidimensional CDF. Complex domain topology is more clearly displayed in the CDF than in the IDF. The CDF method is presented in Sect. 8.5.5.

**Definition.** The interface distribution function

$$g_1(x) = - \left( \frac{d\rho_1(x)}{dx} \right)^{*2} = -k\gamma_1''(x) \quad (8.72)$$

is proportional to the 2nd derivative of the related 1D correlation function,  $\gamma_1(r)$  (cf. Sect. 8.5.2).

**Computation.**  $g_1(x)$  is computed from any 1D scattering intensity, e.g.  $I_1(s_3)$

<sup>85</sup>A more complex model can be constructed from two components or a special sequence of (thick and thin) layers.

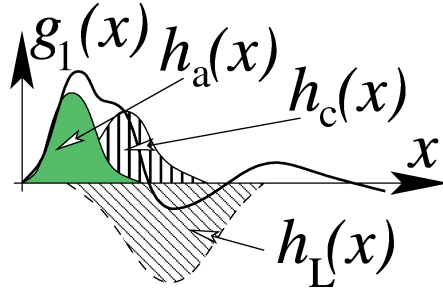


**Figure 8.25.** The features of a primitive interface distribution function,  $g_1(x)$ . The IDF is built from domain thickness distributions,  $h_a(x)$  and  $h_c(x)$ , followed by the distribution of long periods,  $h_L(x)$ , and higher multi-thickness distributions

$$g_1(x) = -\mathcal{F}_1 \left( 4\pi s_3^2 I_1(s_3) - \lim_{s_3 \rightarrow \infty} 4\pi s_3^2 I_1(s_3) \right) \quad (8.73)$$

$$= -\mathcal{F}_1(G_1(s_3)) \quad (8.74)$$

by 1D Fourier transform. It is permitted to replace  $I_1(s_3)$  by any<sup>86</sup> 1D projection  $\{I\}_1(s_i)$  of a deliberate scattering pattern. The function which is subjected to the Fourier transform is identified as a 1D interference function,  $G_1(s_3)$  (cf. page 140, Eq. 8.59).

**Interpretation.** Similar to the CLD,  $g(r)$  (constructed from a series of segment distributions), the IDF,  $g_1(x)$  is a series of thickness distributions,  $h_i(x)$ . While the CLD lumps together all the segments that penetrate a domain in any deliberate direction, the IDF is more selective. Here a specific direction is chosen. Two examples:  $x$  is the coordinate in the direction of the principal axis of the scattering entities;  $r_3$  is the coordinate in fiber direction.

Thus, in the special case of a layer stack morphology,  $g_1(x)$  is a series of thickness distributions (cf. Fig. 8.25). The series starts from the thickness distributions of “amorphous” and “crystalline” layers,  $h_a(x)$  and  $h_c(x)$ , respectively. It is continued by the distributions of *aggregates* of adjacent layers, the first being an aggregate of one amorphous and one crystalline layer. The corresponding di-thickness distribution,  $h_L(x) = h_{ac}(x) + h_{ca}(x) = 2h_{ac}(x)$  shows up with negative sign and represents the long periods. Thereafter we have the tri-thickness distributions  $h_{aca}(x)$ ,  $h_{cac}(x)$ , and the following multi-thickness distributions.

Let us consider the other example. In an anisotropic material we select the fiber axis,  $r_3$ , project the intensity on this direction and compute an IDF. Then the meaning of the thickness distributions is quite similar as in the aforementioned example. Let us identify the first thickness distribution,  $h_h(r_3)$ , by a distribution of hard-domain thicknesses. Then the next thickness distribution,  $h_s(r_3)$ , is the thickness distribution

<sup>86</sup>That is, the direction of the projection may be chosen deliberately.

of the soft material in between, and the long period distribution is  $h_L(r_3) = h_{hs}(r_3) + h_{sr}(r_3) = 2h_{hs}(r_3)$ .

As we proceed from distribution to distribution within the series of thickness distributions, we observe that the functions are growing broader and broader. Moreover, their sign is alternating<sup>87</sup>, and in a material with short-range order the IDF is already vanishing for relatively small values of  $x$ ,  $r_3$  or another chosen direction.

This observation is expected from theory, as the observed thickness distributions are exactly the functions by which one-dimensional short-range order is theoretically described in early literature models (ZERNIKE and PRINS [116]; J. J. HERMANS [128]). From the transformed experimental data we can determine, whether the *principal* thickness distributions are symmetrical or asymmetrical, whether they should be modeled by Gaussians, gamma distributions, truncated exponentials, or other analytical functions. Finally only a model that describes the arrangement of domains is missing – i.e., how the *higher* thickness distributions are computed from two principal thickness distributions (cf. Sect. 8.7). Experimental data are fitted by means of such models. Unsuitable models are sorted out by insufficient quality of the fit. Fit quality is assessed by means of the tools of nonlinear regression (Chap. 11).

**Warning.**  $g_1(0) \geq 0$  must hold. If in an experimentally determined curve  $g(0)$  or  $g_1(0)$  becomes strongly negative, there is a shortcoming in the pre-evaluation of the data. Probably the error originates from incorrect absorption correction or from errors in a manual evaluation of the Porod region. If a manual “deconvolution” of  $g_1(x)$  is carried out, the areas of the peaks must conform to a zero-sum rule (cf. p. 158), and the centers of gravity of the peaks must conform to the obvious law of addition (e.g.,  $\bar{d}_c + \bar{d}_a = \bar{L}$  for the average crystalline thickness, the amorphous thickness and the long period). These constraints are not easily maintained manually, but can be programmed into a model function with little effort. Thus the constraints aggravate a manual evaluation of the IDF, but assist the deconvolution if methods of nonlinear regression are applied: even for rather diffuse IDFs unique deconvolutions can be found, if the type of the thickness distributions and the statistical model (Sect. 8.7) of domain arrangement is known. If distribution type and statistical model are varied, the results of the fits are discriminated by the quality of the match.

## 8.5.5 Anisotropic Chord Distribution Functions (CDF)

### 8.5.5.1 Definition

The anisotropic multidimensional chord distribution (CDF) is an advancement of the IDF which is adapted to the study of highly anisotropic materials. CLD, IDF, and CDF are all based on the edge-enhancement principle devised by MÉRING and

<sup>87</sup>A negative long-period peak is always accompanied by two positive satellite peaks with each half the area (simplified zero-sum rule). Remember the alternating signs of the  $\delta$ -functions in Fig. 8.24 and have a look at p. 158.

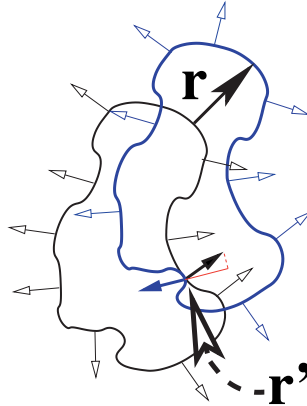


**Figure 8.26.** A particle–ghost autocorrelation of *gradient vectors* is generating the CDF. The vectors are emanating in normal direction from the surfaces of the particle and its ghost. The ghost is displaced by the vector  $\mathbf{r}$ . The dashed arrow points at the position  $\mathbf{r}'$ , at which a contribution to the CDF is generated. It originates from the scalar product of the two gradient vectors drawn in bold

TCHOUBAR. For the application to anisotropic scattering patterns STRIBECK [26] has extended this principle to a space of deliberate dimensionality. Available technology constricts its practical use to the scattering of materials with fiber symmetry, and the fiber-symmetrical CDF

$$z(r_{12}, r_3) = (\nabla \rho(r_{12}, r_3))^{\ast 2} = k \Delta \gamma(r_{12}, r_3) \quad (8.75)$$

is closely related to VONK's multidimensional correlation function,  $\gamma(r_{12}, r_3)$  ([168] and [22], p. 302). One could think of synthesizing the CDF from a complete set of IDFs according to RULAND [66], but a viable algorithm for this path has not yet been found.

In space the 1D derivative  $d/dx$  is replaced by the gradient  $\nabla$ , as is the second derivative  $d^2/dx^2$  by the Laplacian  $\Delta$  [26]. In analogy to the particle-ghost construction of the correlation function (cf. Figs. 2.4 and 8.24) the construction of the CDF can readily be demonstrated (Fig. 8.26). In a multiphase material the gradient field  $\nabla \rho(\mathbf{r})$  is vanishing almost everywhere. Exceptions are the domain surfaces. They are densely populated with gradient vectors, the lengths of which are proportional to the heights of the density jumps.

### 8.5.5.2 Computation of the CDF for Materials with Fiber Symmetry

CDFs are computed from scattering data which are anisotropic and complete in reciprocal space. Thus the minimum requirement is a 2D SAXS pattern of a material with fiber symmetry taken in normal transmission geometry (cf. p. 37, Fig. 4.1). Required pre-evaluation of the image is described in Chap. 7.



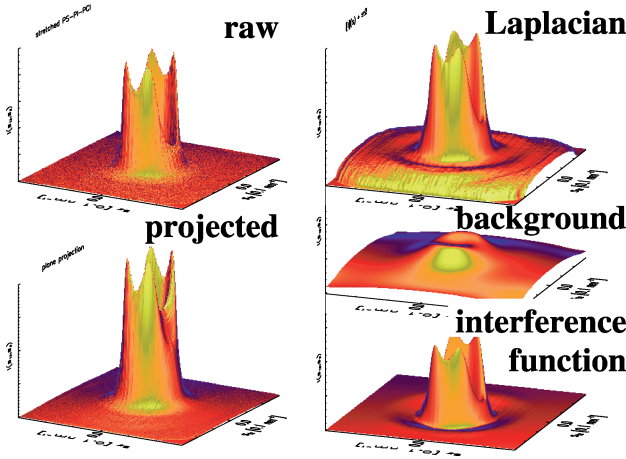


**Figure 8.27.** Steps preceding the computation of a CDF with fiber symmetry from recorded raw data: The image is projected on the fiber plane, the equivalent of the Laplacian in real space is applied, the background is determined by low-pass filtering. After background subtraction the interference function is received

**Transformation of the Pre-evaluated Image.** The image  $I(s_{12}, s_3)$  is projected on the representative plane  $(s_1, s_3)$  of the fiber scattering<sup>88</sup>

$$\{I\}_2(s_1, s_3) = 2 \int_0^\infty I\left(\sqrt{s_1^2 + s_2^2}, s_3\right) ds_2. \quad (8.76)$$

By means of this procedure our problem is not only reduced from three to two dimensions, but also is the statistical noise in the scattering data considerably reduced. Multiplication by  $-4\pi s^2$  is equivalent to the 2D Laplacian<sup>89</sup> in physical space. It is applied for the purpose of edge enhancement. Thereafter the 2D background is eliminated by spatial frequency filtering, and an interference function  $G(s_{12}, s_3)$  is finally received. The process is demonstrated in Fig. 8.27. 2D Fourier transform of the interference function

$$z(r_{12}, r_3) = -\mathcal{F}_2(G(s_{12}, s_3)) \quad (8.77)$$

finally yields the CDF,  $z(r_{12}, r_3)$ .

### 8.5.5.3 Relation Between a CDF and IDFs

Every radial, 1D slice through the center of a CDF

<sup>88</sup>The reason for this projection is that we are interested in the study of *slices*  $\gamma(r_1, r_3) = \frac{1}{k} \mathcal{F}_2(\{I\}_2(s_1, s_3))$  in *real space*. So we must project in reciprocal space in order to reduce the fiber-symmetrical problem from three to two dimensions.

<sup>89</sup>Conceded – there is the alternative to apply a 3D Laplacian, but the corresponding procedure turns out not to be as stable as the 2D Laplacian when applied to experimental data.

$$[z]_1(r_{\psi,\varphi}) = g_1(r_{\psi,\varphi})$$

is an IDF by definition. In the equation the slicing direction is indicated by a polar and an azimuthal angle,  $\psi$  and  $\varphi$ , respectively. Of particular practical interest for the study of fibers is the cut of the CDF along the fiber axis,

$$[z]_1(r_3) = z(0, r_3) = g_1(r_3),$$

which describes the longitudinal structure of the material (cf. Sect. 8.4.3.2). In analogous manner the transversal structure (cf. Sect. 8.4.3.3) of the fiber is described by the slice

$$[z]_2(r_{12}) = z(0, r_{12}) = g_2(r_{12})$$

of the CDF. A typical CDF of a highly oriented semicrystalline polymer material is shown in Fig. 8.28. Viewed from the top the domain peaks are visible, whereas viewing a CDF from the bottom shows the long periods peaking out.

#### 8.5.5.4 How to Interpret a CDF

A CDF is interpreted in the same way as a CLD or an IDF. All these functions exhibit the probability distributions of domain size and arrangement. Clearer than a CLD is the IDF, because it does not contain an orientation average but exhibits the topology in a selected direction. Clearer than an IDF is the CDF, because it visualizes the nanodomain topology in space, i.e., in more than one direction.

**Uncorrelated Particles: Only Positive CDF Peaks.** Let us consider the simple example of identical, highly oriented cylinders which are randomly distributed in the material. Figure 8.29 demonstrates the scheme for the construction of the CDF assuming that the cylinder axis is parallel to the fiber axis. Two strong peaks on the meridian with almost triangular shape are characteristic for the cylinder. The *signal height* at a position  $\mathbf{r}$  (i.e., at the position of the “glass rod” on the front peak in the sketch) is proportional to the area of contact between the cylinder and its displaced ghost. The basis length of the triangle is twice the *diameter* of the cylinder. The thickness of the triangle in meridional direction reflects the *polydispersity* of cylinder heights in the material. In addition, two weak diameter peaks are observed crossing the equator of the CDF. They are formed as the ghost is passing along the side of the particle.

The results of these considerations are readily extended from cylinders to lamellae: in the latter case the strong triangular peaks are wider, but closer to each other.

**Arrangement of Particles and the Corresponding Peaks.** If a CDF shows only positive peaks, the particles in the material are distributed at random<sup>90</sup>. There is no arrangement. Growing correlations are indicated by one or more triplets of peaks

<sup>90</sup>The reverse is only true for particles whose shape is *convex*, i.e., if the particles do not contain holes or indentations.

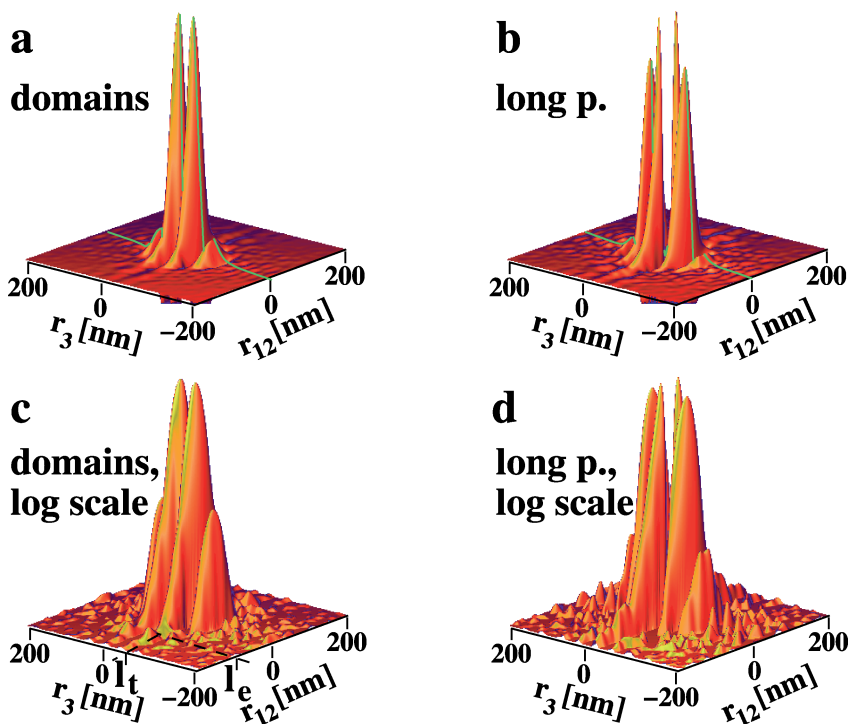


**Figure 8.28.** Demonstration of a CDF. Data recorded during non-isothermal oriented crystallization of polyethylene at 117°C. Surface plots show the same CDF: (a) Linear scale viewed from the top. (b) Linear scale viewed from the bottom. (c) Viewed from the top, logarithmic scale. Indicated are the determination of the most probable layer thickness,  $l_t$ , and of the maximum layer extension,  $l_e$ . (d) Viewed from the bottom, logarithmic scale. The IDF in fiber direction is indicated by a light line in (a) and (b) (Source: [56])

which do not change the integral of the CDF [172]. Let us demonstrate this general *zero-sum game of growing correlation* in one dimension by consideration of the IDF (Fig. 8.30). For every particle added to the structural entity, three additional peaks are observed. Their integral is zero<sup>91</sup>.

From a practical point of view the sign of a peak in CLD, IDF, or CDF is described by the character of surface contact between particle and ghost<sup>92</sup>: if they contact each other in the normal way, the peak is positive; it is negative if they penetrate each other at the considered surface. Thus, positive peaks describe the size of par-

<sup>91</sup>I came across the zero-sum rule of correlation when I started to program models for structure fitting. Structure models which violate the zero-sum rule cannot be fitted to experimental data. Their convergence is poor.

<sup>92</sup>Up to now we have only discussed the correlation of a particle with *its own* ghost. In general, arrangement means that correlations between a particle and ghosts of *other particles from the same phase* are not extinguished by random annihilation.

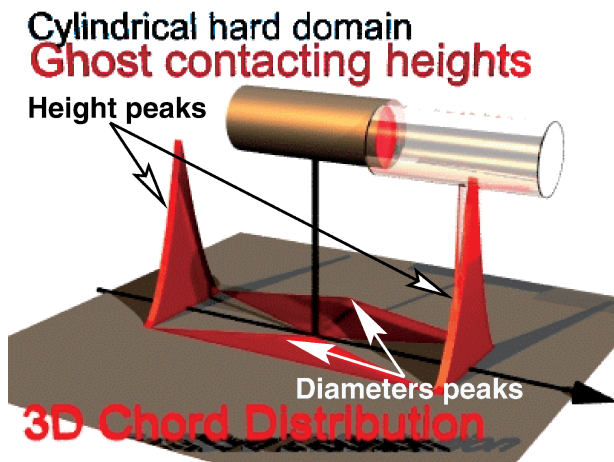


**Figure 8.29.** A particle-ghost displacement-principle governs the relation between structure and CDF. The height of the CDF signal is proportional to the *area of contact* between the particle and its ghost. A bold arrow in the base plane indicates the meridian (fiber direction)

ticles or super-particles. Negative peaks describe the space that is controlled by a particle or a super-particle from the structural entity. If the topology is addressed as a lattice, negative peaks show up at every repeat of the lattice constant (long period). If no long periods are detected, the structure describes an ensemble of uncorrelated particles. Every CDF analysis starts from such considerations.

#### 8.5.5.5 Semi-quantitative CDF Analysis. An Example

**The Material of the Example.** Poly(ether ester) (PEE) materials are thermo-plastic elastomers. Fibers made from this class of multiblock copolymers are commercially available as Sympatex<sup>®</sup>. Axle sleeves for automotive applications or gas-kets are traded as Arnitel<sup>®</sup> or Hytrel<sup>®</sup>. Polyether blocks form the soft phase (matrix). The polyester forms the hard domains which provide physical cross-linking of the chains. This nanostructure is the reason for the rubbery nature of the material.

**Synopsis of Experiment and Results.** The material is irradiated during straining and relaxation. The example shows that a nanostructure which is hard to interpret from a series of scattering patterns may clearly reveal its complex domain structure after transformation to the CDF. Different structural entities are identified which respond each in a different way on mechanical load. The shape of the basic particles is identified (cylinders). The arrangement of the cylinders is determined. Thus the semi-quantitative analysis of the CDF provides the information necessary for the selection and definition of a suitable complex model which is required for a

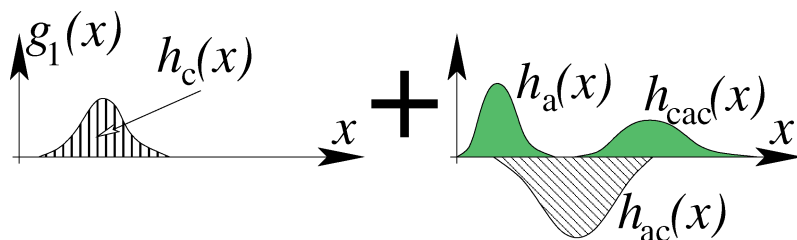


**Figure 8.30.** From particles to complex scattering entities in the IDF, the CDF or the CLD by growing correlation: An ensemble of uncorrelated particles exhibits only one homo-segment distribution (e.g.,  $h_c(x)$  representing crystallites). As next-neighbor correlations are growing, three segment distributions are added. *The integral of this triplet is zero.* Growing range of correlation adds further triplets

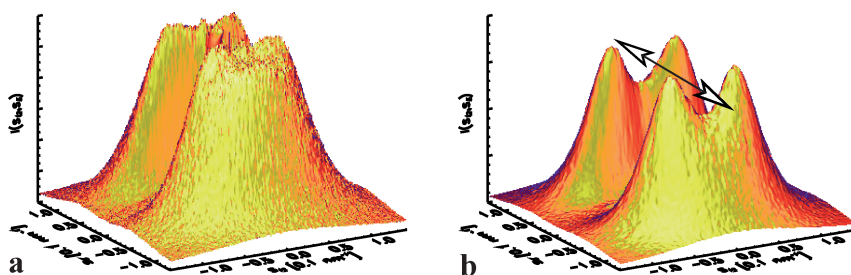


**Figure 8.31.** Fiber scattering of PEE 1000/43: (a) at an elongation  $\epsilon = 0.88$ ; (b) during relaxation from  $\epsilon = 0.88$ . The fiber direction is indicated by a double-arrow. Visualized region:  $-0.15 \text{ nm}^{-1} \leq s_{12}, s_3 \leq 0.15 \text{ nm}^{-1}$ .  $\epsilon = (l - l_0)/l_0$ , with  $l_0$  and  $l$  defined by the initial and the actual distance between two fiducial marks on the sample

complete quantitative analysis<sup>93</sup>. Even without a complete analysis mechanisms of structure evolution can be detected, if SAXS measurements are carried out *in situ* during processing by application of load (thermal, mechanical, ...).

Figure 8.31 shows central sections of two original SAXS patterns of PEE 1000/43<sup>94</sup> in strained and relaxed state. In the strained state (Fig. 8.31a) a “6-point-diagram” is detected. During relaxation (Fig. 8.31b) a well-separated “4-point-diagram” is observed. Interpretation of the patterns is restricted to description and speculation.

<sup>93</sup>In 3D a quantitative analysis still appears to be hopelessly laborious because of the complexity of the problem. On the other hand, a 1D quantitative analysis of only the longitudinal structure can be mastered (cf. Sect. 8.7).

<sup>94</sup>PEE's are commonly characterized by two numbers (e.g., 1500/50). The first number reports the minimum quantization of the polyether blocks (meaning “the polyether blocks are multiples of 1500 g/mol”), the second number indicates the mass fraction of the polyester hard phase (e.g., 50 wt.-% of polyester).

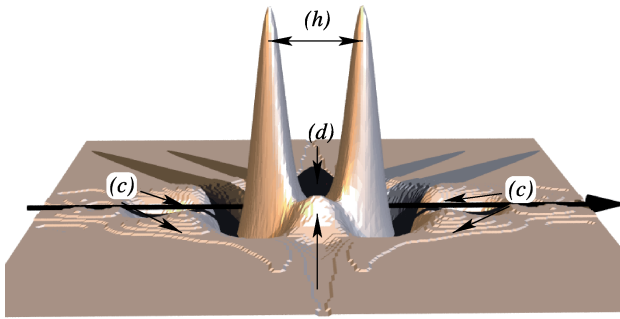


**Figure 8.32.** PEE 1000/43 at  $\varepsilon = 0.88$ . CDF  $z(\mathbf{r})$ . The domain peaks are pointing upwards: (h) cylinder-height peaks; (d) cylinder-diameter peaks; (c) inter-domain correlation peaks. Displayed region:  $|r_{12}, r_3| \leq 40$  nm

In an original paper [173] the longitudinal structure has been studied quantitatively as a function of elongation. In a follow-up study [174] the 3D CDF has been computed and analyzed. Figure 8.32 shows the 3D CDF with fiber symmetry computed from the scattering pattern in Fig. 8.31. The straining direction  $r_3$  is indicated by the long arrow in the basic plane. The observer is facing the domain peaks. Close to the origin the strong peaks on the meridian (h) mark the correlation between opposite faces of the basic domains. Two equatorial peaks (d) indicate the diameter of the domains. Because the height-to-diameter ratio is greater than 1, the basic domains can be approximated by *cylinders*. Four correlation peaks (c) are observed in an oblique angle with respect to the fiber axis. They indicate arrangement of domains. Their position shows that the closest neighbors of a cylinder are not found in straining direction, which would be indicative of a microfibrillar arrangement. Instead, the cylinders form a cluster with 3D short-range correlation. Such structural entities have been called a *macrolattice* by WILKE [175, 176]. The discussed peaks carry positive sign, because they describe chords that reach from the front face of a cylinder to the back face of a neighboring domain. The corresponding long periods show up as indentations observed at a shorter distance from the center, as they are measured “from front to front” of the domains. They are more easily observed after the CDF has been turned upside-down (Fig. 8.33). Obviously the long periods in fiber direction (a) are less pronounced than the long periods in oblique direction (b). Moreover, the CDF shows that the topology does not contain long-ranging correlations among domains. In fiber direction there is a long period of 25 nm (a), but already the size of the domain behind it can no longer be determined. On the other hand, the arrangement of domains in oblique direction (b) shows better correlation: here not only the long period, but also the size of the cylinder behind it can be determined (Fig. 8.32, (c)).

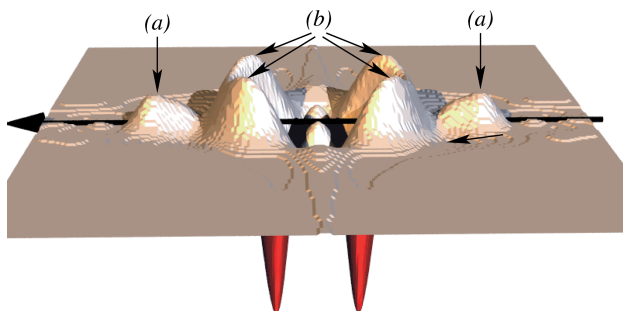


**Figure 8.33.** CDF  $-z(\mathbf{r})$  of PEE 1000/43 at  $\varepsilon = 0.88$ . The long-period peaks are pointing upward: (a) long period to the next neighbor in straining direction; (b) stronger long period to the closest neighbor (in oblique direction)

During the beamtime another scattering pattern has been exposed after unloading the material. The respective CDF is shown in Fig. 8.34. Compared with the data from the strained state, the positions of the oblique long periods do not move (b). This finding indicates that the central cylinders are surrounded by domains which are rigidly coupled to them. In the scattering pattern such a structural entity is not easily discriminated from the 4-point diagram of a stack of inclined lamellae. In this respect the CDF is much clearer.

How should such rigid domain coupling work? In principle domains can only be rigidly coupled by a bridge of hard-phase material which has a different density. We know that the polyester hard-phase is semi-crystalline. So the observation is indicative for a structure in which the hard domains are subdivided into crystalline and amorphous zones. Thus a quantitative model of the structure would probably require to consider a third phase (*three-phase system*).

Finally we can compare the nanostructure in fiber direction after unloading with the nanostructure observed under mechanical load. The most striking variation is related to the strong long period (a), which is relaxing to half the value found in the elongated state. In addition to the strong long period, only in the unloaded material another long period is found (a'), for which even the 2nd order is visible. Thus the corresponding structural entities are built from domains with already a considerable range of correlation which are arranged along the straining direction. This is just the topological definition of a *microfibril* [157]. As the material becomes strained, the softer matter between the domains is elongated by different amounts and the longitudinal correlation gets lost. Thus the semi-quantitative analysis of the CDF returns a detailed view on the nanostructure evolution under load. More examples of

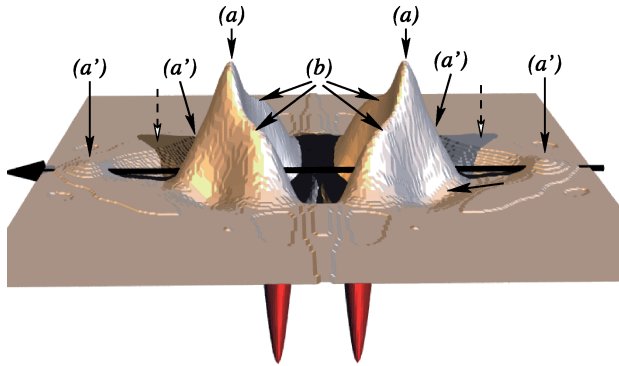


**Figure 8.34.**  $-z(\mathbf{r})$  for PEE 1000/43 recorded during relaxation of the material from a first elongation to  $\varepsilon = 0.88$ . (a) strongest long-period in straining direction (13 nm) (dashed arrows with white head indicate the old positions of these peaks under strain); (a'): the best-correlated long-period in fiber direction (17 nm), because it shows a 2nd order; (b) oblique long period that is immovable in the straining experiment

the CDF method can be found in a growing number of original studies [56, 57, 177–186].

## 8.6 Biopolymers: Isotropic Scattering of Identical Uncorrelated Particles

**Overview.** Considerable research activities in the fields of isotropic SAXS and small-angle neutron scattering (SANS) are devoted to the investigation of ensembles of uncorrelated but identical or almost *identical complex particles*. Frequently these particles are studied in solution. Samples for such investigations must be supplied in a solution in which the particles do not aggregate.

The majority of the research is focused on colloidal and biological materials. In several textbooks [86, 101, 136, 187] the related methods are elaborated. Recent developments are considered in a review of SVERGUN and KOCH [188].

**Classical Analysis.** The classical analytical methods are even applicable for polydisperse samples and rest on the CLD (Sect. 8.5.3) and on VONK's [189] distance distribution function (DDF) ([189–191]; [101] p. 168)

$$p(r) = r^2 \gamma(r). \quad (8.78)$$

Figure 8.35 shows for homogeneous identical spheres the radial correlation function (GUINIER and FOURNET [65] p. 12–19; LETCHER and SCHMIDT [192])



<http://www.springer.com/978-3-540-69855-5>

X-Ray Scattering of Soft Matter

Stribeck, N.

2007, XX, 240 p. With online files/update., Hardcover

ISBN: 978-3-540-69855-5